Dynamic Aspects of Graphene Deformation and Fracture from Approximate Density Functional Theory

Gang Seob Jung[1*], Stephan Irle[1,2] and Bobby Sumpter[3]

[1]Computational Sciences and Engineering Division, Oak Ridge National Laboratory, Oak Ridge, TN 37831, USA

[2]Bredesen Center for interdisciplinary Research and Graduate Education, The University of Tennessee, Knoxville, USA

[3]Center for Nanophase Materials Sciences, Oak Ridge National Laboratory, Oak Ridge, TN 37831 USA

Abstract: Graphene is one of the most intriguing two-dimensional carbon materials. Its mechanical strength and failure are key concerns for materials engineering and applications. Despite the success of fracture mechanics, the mechanism of how pristine materials fail remains an elusive problem. While many theoretical studies based on molecular dynamics using empirical forcefields have tried to address this question, atomic-scale mechanics are not clearly understood. Especially, a widely employed bond-breaking approach based on the critical bond length has not been rigorously tested. Here, utilizing molecular dynamics simulations with density functional based tight binding, we investigate how the failure of the pristine material initiates. The Wiberg bond order (W_{BO}) to estimate the change of chemical bonds shows a transition from sp^2 ($W_{BO} \sim 1.33$) to sp^3 ($W_{BO} < 1.0$) during the deformation. However, it reveals that a single threshold value for either the W_{BO} or bond length is insufficient to decide failure of pristine material without free edges or defects. Instead, collective behaviors of the local atomic group govern the fracture initiation of pristine graphene. Our study provides dynamic mechanical responses based on quantum mechanics, which have not been captured by empirical forcefields, opening opportunities to design properties by precisely coupling the mechanics and quantum mechanics.

Keywords: DFTB, reactive forcefields, molecular mechanics, graphene, fracture

Notice: This manuscript has been authored by UT-Battelle, LLC, under Contract No. DE-AC05-00OR22725 with the U.S. Department of Energy. The United States Government retains and the publisher, by accepting the article for publication, acknowledges that the United States Government retains a

* Corresponding author. Tel: (836) 341-0402. E-mail: jungg@ornl.gov

nonexclusive, paid-up, irrevocable, world-wide license to publish or reproduce the published form of this manuscript, or allow others to do so, for United States Government purposes. The Department of Energy will provide public access to these results of federally sponsored research in accordance with the DOE Public Access Plan (http://energy.gov/downloads/doe-public-access-plan).

1. Introduction

Fracture is a critical concern in materials synthesis, durability, and functionality for various applications. In a brittle material, a sharp crack governs the catastrophic failure through crack propagation [1-3]. Based on Griffith's theory, classical fracture mechanics assumes that materials have flaws that play like a crack in the interior or surface of materials to explain brittle materials' failure [4]. This classical fracture mechanics based on a sharp crack has successfully described the crack propagation combined with atomistic simulations [5]. Therefore, previous studies have focused more on cracks, defects, dislocations, and grain boundaries to understand the mechanical strengths of graphene [6].

In principle, mechanical loading can initiate a sharp crack and catastrophic failure from the pristine regions. However, how such a crack is nucleated in the early stage of failure is still elusive from the fracture mechanics. On the other hand, atomistic simulations have been widely utilized to answer this question based on a specific bond length or cutoff to describe bond breaking to predict the strengths of pristine graphene. Previous computational studies have reported strain and temperature effects on the pristine graphene's strength based on this critical bond length without careful validation and have not made distinct progress [7, 8]. In the meantime, the mechanically or thermally induced bond-breaking and fracture become more vital to synthesis, structural designs, and applications with graphene and other two-dimensional (2D) materials [9-11].

On the other hand, 2D materials have emerged as an ideal platform to investigate the effect of atomic structures such as defects, vacancies, grain boundaries, and crack directions on the mechanistic behaviors of materials by combining large-scale atomistic simulations and advanced transmission electron microscopy (TEM) techniques [12-16]. In the previous studies, the empirical reactive forcefields (FFs) have been extensively utilized to understand fundamental governing mechanisms on crack propagation by systematic comparison with TEM observation.

However, capturing the initiation of failure from the pristine 2D materials is still challenging due to the time resolution and the difficulty in identifying the location of the failure. Therefore, first-principles calculations based on quantum mechanics (QM) such as density functional theory (DFT) become essential to investigate the initiation of failure in pristine materials [17].

In this study, we utilized the density functional based tight binding (DFTB) approach [18], which is an approximate electronic structure method, to overcome the computational demands of DFT in terms of time- and length-scale limitations while conserving quantum mechanical accuracy. This method was recently successfully employed in the static simulation of graphene peak stress and strains [19]. We systematically compared DFT and DFTB calculations under various loading conditions, showing good agreement in terms of deformation and strain stress behaviors. Also, we directly compared them with two classical reactive empirical FFs. To avoid any effects from sizes and loading conditions, we developed an interface between LAMMPS [20] and the DFTB+ [21] software, which will be made available to the public. Finally, we have tested the validity of the critical bond length at various temperatures. The results reveal limitations of the reactive FFs for understanding the pristine materials' failure and imply the importance of the atomic vibrational behaviors to initiate the pristine graphene's failure.

2. Methods

We utilize DFTB+ (Density Functional based Tight Binding) package [21] as a library to calculate force and potentials in the LAMMPS molecular dynamics package [20]. The molecular dynamics simulations with DFTB and empirical FFs were performed *via* the LAMMPS package. We utilized Quantum Espresso (QE) [22, 23] to perform DFT calculations with the pseudopotentials library [24].

2.1 DFT for mechanics and deformation of graphene

We prepared a rectangular unit cell of graphene having four atoms in Figure 1(a) with periodic boundary conditions to obtain stress-strain curves and atomic distortion under the static loading. The projector augmented-wave (PAW) method [25] with Perdew-Burke-Ernzerhof (PBE) functional [26] and an energy cutoff for the plane waves set as 40 Ry was used. The Brillouin

zone was sampled using a 13x13x1 Monkhost-Pack grids for the K space sampling. For the slab system, we used a 15Å vacuum space to avoid the interaction between periodic images.

After structural relaxations, we apply a static loading along the *x* direction (zigzag: *zz*) and *y* direction (armchair: *ac*). We sequentially stretched the box with $\Delta\varepsilon = 0.01$ with the structural relaxation to obtain the stress. During the structural relaxation, we do not change the box dimension for the plane strain condition. The geometries and stress along both directions were recorded as reference data. The thickness of graphene was assumed to be 3.35Å [27]. We utilized the BFGS quasi-newton algorithm to relax the structure with a convergence threshold on the force as 1.0 e-3 (Ry/Bohr) *via* QE.

2.2 DFTB calculation of different parameters

We utilized three different C-C parameters for DFTB calculations to compare: MIO [28] with the second-order DFTB2 scheme, 3OB [29] with the third-order DFTB3 scheme, and OB2 that were developed for the LC (long-range corrected)-DFTB2 scheme [30]. We note that we did not utilize the long-range correction with the LC-DFTB2 scheme because periodic boundary conditions are not currently available for this method. LAMMPS calls force and potentials based on the geometries and simulation box from the DFTB+ library during the MD simulations. We compared stress-strain curves from the parameters with DFT calculations. Then, the 3OB parameter is chosen for the further investigation of graphene's mechanical properties. We mainly tested with the 3OB parameters for the dynamic loading and further splits, such as strain rate, temperature, and Fermi temperature to confirm the conditions for the comparison, as shown in Figures S1 and S2. Table 1 shows the details set-up for DFTB+ inputs. After checking the size effects with k sampling, we prepare a 20 x 20 Å graphene sheet and 33.5Å space along the *z* direction with a periodic boundary condition for DFTB calculations.

2.3 Wiberg's bond order

We utilized bond order to estimate the change of chemical bonds during the deformation. The Wiberg bond order index is given by [31]

$W = \sum_{\mu \in A} \sum_{\nu \in B} |D_{\mu\nu}|^2$,

where $D_{\mu\nu}$ is the elements of the density matrix obtained from occupied orbital coefficients ($C_{\mu i}$) as $D_{\mu\nu} = 2\sum_{i}^{OCC.} C_{\mu i} C_{\nu i}^{*}$.

2.4 Empirical reactive forcefields

We tested ReaxFF and AIREBO which have been utilized to understand the deformation and fracture mechanics of graphene at the atomic to compare the results from DFTB+. For the ReaxFF, we used the version of ReaxFF- C_{2013} [32] that has been developed to account for the mechanical response of carbon materials, including graphene and diamond, and have shown improvements to predict mechanical properties compared to the previously developed ReaxFF-CHO [33]. For the AIREBO[34, 35], it is critical to modify cutoffs as $R_{min} = R_{max} = 2.0$Å to remove the unphysical stiffening effects near the failure points [36] and utilized in graphene-related materials [37, 38]. We prepared the same size of graphene with DFTB+ under the same loading conditions.

2.5 Quasi-static loading

Static loading shows a larger critical strain than the dynamics loading from both DFTB and empirical FF calculations. For dynamic loading, finite temperature distorts deformation that is strongly imposed by the energy minimization. To obtain failure points with dynamic loading with reduced steps, we used the quasi-static loading. In this loading style, we include ten steps of the NVT ensemble to allow variation of the geometries from a finite temperature (10 Kelvin) at each stretch ($\Delta\varepsilon = 0.01$). We tested different numbers of integration from 10 to 100 in Figure S3 to confirm the conditions. We set 0.0 and 1.0e-8 for the energy and force tolerance for the conjugate gradient minimization in DFTB and MM calculations, respectively, which is adequate for reliable stress-strain curves under static loadings.

2.6 Quasi-dynamic loading

While the quasi-static loading can capture the failure points like dynamic loading, the different dynamics caused by the varying temperature are not captured due to the energy minimization. We thus stretched the system with a particular strain level and then applied dynamic loading after structural relaxation and equilibrium run at a given temperature. We performed 1000 steps for the equilibrium after energy minimization for both DFTB and empirical FFss. The same

conditions, such as a thermostat, damping coefficient, and loading speed (10m/s), were applied to remove any undesired effects from MD settings. We allowed enough deformation (~0.01) strain (several thousands of steps) before fracturing for pristine graphene to have enough time to adjust themselves with a given temperature under dynamic loading.

2.7 LAMMPS code development for DFTB+

The open-source package, DFTB+ [21], provides API for other codes in both Fortran and C++. We follow the same strategy utilized in the LATTE package developed by Dr. Christian Negre (Los Alamos National Laboratory), using the "fix" command provided in LAMMPS to incorporate the energy, force, and virial term called from DFTB+ package. Users can couple the current code with various packages: the COLVAR package [39] for the advanced sampling methods such as Meta-Dynamics and Adaptive Bias Force method; REPLICA package for the replica-exchange MD and Nudged Elastic Band (NEB) methods; User-MISC package for Steered Molecular Dynamics (SMD).

3. Results and Discussions

One of the most challenging parts to compare mechanical deformation and failure at the atomic scale from different methods such as DFT, DFTB, and reactive FFs, is the difference of the accessible length and time scales. Since the loading conditions and system sizes can affect the failure behavior, we carefully define different loading conditions: static loading, dynamic loading, quasi-static loading, and quasi-dynamic loading. Figure 1(a) shows the system sizes and loading directions applied to pristine graphene with periodic boundary conditions in this study.

Firstly, we checked the stress-strain behavior under tensile loadings obtained from DFTB with three available C-C DFTB parameters (labeled MIO, 3OB, and OB2) through a comparison with full DFT calculations as shown in Figure S4. MIO and OB2 were employed in second-order DFTB [28], whereas the 3OB parameter was utilized in third-order DFTB parameters. We utilized static loading under the plane strain condition for both DFT and DFTB. We investigated the origins of the different failure behaviors and deformation by checking the shapes of the C-C

potentials and the first derivatives, as shown in Figure S5. In this comparison, we found that there is a stiffening behavior of stress-strain curves with the MIO parameter under static loading at the strain level between 0.1 and 0.15. Such behavior is, in fact, commonly observed with REBO or Tersoff types of empirical potentials due to the use of a switching function that makes the potential stiffer near the failure point [36]. The stiffening comes from the first derivative of the energy with a bump shown in the bond length between 1.6 Å and 1.8 Å in Figure S5b. We note that the energy difference from the expected smooth curve is relatively tiny, around 0.2 eV compared to the minimum energy around -10 eV (~ 2%). However, the first derivative shows a significant difference (more than 2 eV/Å, mainly from the repulsive potential force, which is around 20% of the maximum force value). This results in 20% enhanced strength, which will significantly affect toughness.

The results imply that the first derivative of the energy (forces) is the most critical property governing the dynamic behaviors for the failure of the graphene systems, and consequently requires careful check and development in parameterizations of the C-C interaction potential. Our findings suggest that there is a possibility to further refine the parameters without significantly modifying the energy to optimize the stress-strain curves closer to DFT calculations. However, such further optimization is out of scope in this study. Therefore, we utilize the third-order DFTB3 method with the 3OB parameter as a reference for the DFTB calculations.

Static loading simulations do not include the effect of atomistic vibration induced by a finite temperature. They suffer from artificially imposing symmetry on the deformation due to the minimization process. Therefore, we introduced quasi-static loading to capture the failure point. Quasi-static loading can approximate the failure strain well compared with dynamic loading, as shown in Figure S6. Also, it can better describe the fracture patterns in Figure S7 than static loading. The deformation under static loading usually shows much higher failure strains compared to the dynamic loading due to the imposed symmetry. The thermal fluctuation due to the finite temperature (here set to 10 Kelvin) under dynamic loading disturbs the symmetry and can predict similar failing strains as the dynamic loading.

For a more realistic description, we then increased the system size in the DFTB simulations from 24 atoms to 240 atoms (See Table 1 for the specific conditions) under the quasi-static loading to see any size effects on failure strains. We compared the stress-strain curves under tensile loadings with different system sizes and k grid points in Figure S8. Then, the size 20 Å x 20 Å (160 carbon atoms) in Figure 1(a) was selected to compare the deformation and fracture with reactive FFs. We defined three different bond lengths and angles shown in Figure 1(b) to analyze the deformation as a function of the applied strain. Figure 2 shows that DFTB3/3OB agrees very well with DFT calculations in terms of stress-strain curves, bond lengths, and angles, confirming earlier an report[19]. Before we explored fracture and deformation under the tensile and shear loading from DFTB and reactive FFs, the elastic constants were obtained and compared in Table 2. A recent study has compared available FFs and DFT for their elasticity [40], which agrees well with our calculations. Since DFTB is an electronic structure method based on atom-centered atomic orbitals, we utilized the Wiberg bond order index W_{BO}[41] to estimate the change of chemical bonds during the deformation. Figure 3(a) shows the distributions of W_{BO}. In the unstrained geometry, all bonds carry an identical W_{BO} of 4/3 in agreement with the distribution of Clar resonance structures [42]. Two different types of bonds can be distinguished as the tensile strain is applied. It allows to clearly identify changes due to the applied strain along the *x* and *y* directions. For one type of bond, the W_{BO} values fall below 1.0, while for the other the W_{BO} values increase beyond the equilibrium value. The obtained charge density also confirms that there is a significant change in charge distribution between bonds, as shown in Figure 3(b). The shortened bond lengths (l_2 along the x direction and l_1 and l_3 along the *y* direction in Figure 2) can be interpreted as localized electrons in a double bond (sp^2). Similarly, the maximum bond lengths are observed for the elongated one about 1.72 ~ 1.75 Å, where the bonds are close to a formal C-C single bond.

Here, we note that the DFT and DFTB calculations both describe the bond length (l_2) decreases from around $\varepsilon_{xx} = 0.05$ in Figure 2(a), which the AIREBO completely fails (monotonical increase without decrease) to describe the deformation as shown in Figure 4(a). However, the stress-strain curves and failure strain from AIREBO relatively work well. The angles are more deformable from AIREBO about 5 ~ 10° compared to DFT(B), and this allows larger failure strains. This mismatch may be ok for describing failure strain and strength. However, the sequences of bond

breaking for crack propagation can be significantly affected by the mismatch. A recent study showed that a small difference of lattice deformation at the crack tip can change fracture patterns, fracture dynamics, and fracture toughness [15]. In previous studies [43, 44], the crack propagation of graphene using AIREBO reported a zigzag pattern along the armchair direction (under the *zz* loading direction), and higher fracture toughness than the other direction (under the *ac* loading direction). Future studies should be able to benefit from utilizing DFTB to carefully check crack behaviors and fracture toughness.

On the other hand, the ReaxFF-C_{2013} can describe the change of l_2 r reasonably before the maximum stress, as shown in Figure 4(c, d). Furthermore, the angle deformation is also well described. However, the stress-strain curves from ReaxFF-C_{2013} are quite different from DFT. ReaxFF-C_{2013} overestimates the strength of more than 50%, and there is a stiffening effect between 0.03 ~ 0.07 strains. While AIREBO provides a clear bond-breaking criterion from a cutoff, ReaxFF-C_{2013} relies on the fitting parameters and the electron charge estimations based on the geometries [45, 46]. The results show that the FFs still have limitations for correctly describing failure points, non-linearity of stress-strain, and deformation of graphene. Therefore, it requires care to utilize those FFs. Also, a better FF for the dynamics needs to be developed to account for failure or fracture. Overall, our results show that DFTB can provide efficient and accurate reference data for multiscale approaches that use empirical or neural network (NN) based FFs.

Next, we explored deformation and fracture under shear loadings. Unlike tensile loading, shear deformation is more sensitive to size due to the out-of-plane deformation and its periodicity. Therefore, we firstly compared the in-plane (the *xy* plane) deformation from DFT and DFTB. Then, we utilized DFTB as a reference for the deformation to compare reactive FFs using the same size. Figure 5 shows stress-strain curves and deformation under the *xy* and *yx* quasi static shear loadings. All three bond lengths and angles of DFTB with the in-plane constraint are well-matched with DFT calculations, as shown in Figure 5(a, b). Figure 5(c, d) shows the geometries with out-of-plane deformation during the shear loadings. Like tensile loading, there is a transition of the bond l_1 to single-bond.

When the out-of-plane deformation is allowed, it forms wrinkles from around the strain, $\varepsilon = 0.04$. Compared to the in-plane deformation, wrinkles from shear deformation prevent strongly shortening bonds of l_2 and l_3, as shown in Figure 5(c, d). The reactive FFs show similar limitations for tensile loading in Figure S9. Under the shear loadings, the AIREBO appears to better describe angular deformation under shear deformation, shear strength, and critical strains than ReaxFF-C_{2013}. Figure 6 shows the distributions of Wiberg's bond order (See Methods) and the out-of-plane deformation. Now there are three groups of bonds due to shear deformation. The critical shear strain under the shear loading along the *xy* direction is shorter than the *yx* direction with the in-plane constraint.

We have checked whether the bond lengths and W_{BO} have any relation from all loading conditions. Figure S10 shows the values of W_{BO} and bond lengths from three bonds from l_1 to l_3. It shows that there is a trend that a longer bond length has a lower value of W_{BO}. However, there is no simple representative function *e.g.*, linear function for the relation between the bond order and the bond length. Furthermore, the critical length of a single bond (the most elongated bond) also changes with the other bonds' status, which strongly implies that a simple criterion of a bond length for the failure is problematic to understand the initiation of pristine graphene fracture.

Finally, we systematically tested temperature effects on the critical strain and strength under tensile loadings. Since the fracture behaviors are not well captured with ReaxFF-C_{2013}, we only compared DFTB and AIREBO. We utilized quasi-dynamic loading to see the kinetic effects of temperature on the initiation of failure. The loading is stretching a system with a strain less than a critical strain and then applying dynamic loading after equilibrium steps at a given temperature.

Figure 7 shows the results under the quasi-dynamic loading along the *zz* and *ac* direction with DFTB and AIREBO with different temperatures from 100K to 1000K. The strength and the critical strain from DFTB are less sensitive than AIREBO. While the critical strain can reduce more than 20% in AIREBO at room temperature, DFTB shows less than a 10% decrease at room temperature compared to quasi-static loading. Also, the strength only drops less than 5% with

DFTB, but AIREBO shows a 10% drop at room temperature. We found that such temperature sensitivity of AIREBO comes from the simple bond length criteria.

There is a significant fluctuation of bond lengths from DFTB at the high temperature, as shown in Figure S11a. However, the bond lengths more homogenously change and cannot have more than 2.0 Å at the low temperature. With AIREBO, once one of the bond lengths is longer than 2.0 Å, suddenly the other two bonds become stronger (many-body effect from the bond order), which results in the catastrophic failure of the entire system. Therefore, the bond length cannot be longer than 2 Å even at high temperatures (Figure S11b). In DFTB simulations, such drastic change is suppressed and instead, collective behaviors of large amplitude vibrating atoms govern the initiation of catastrophic fracture in graphene at high temperatures while more homogeneous deformation with smaller amplitudes is observed at low temperature (See Smovies 6-13).

4. Conclusions

In summary, we have systematically investigated the mechanical deformation and fracture of pristine graphene from approximate quantum mechanics calculations (DFTB) and empirical reactive FFs. Previously, there were no systematic and direct comparison at finite temperature with quantum mechanics mainly due to the lack of available tools, while ReaxFF and AIREBO have been broadly utilized to understand the mechanics and fracture dynamics of graphene. In this study, we have developed an interface for the LAMMPS to utilize the DFTB+ package, and therefore, we are able to compare the tensile and shear deformation and fracture behaviors under the same conditions, including thermostats, equilibrium process, system sizes, and loading styles, and other details. Our results reveal limitations of empirical FFs for describing fracture and deformation of pristine graphene. For example, DFTB calculations show that the critical bond length is variable based on the loading conditions and temperatures. Therefore, thermally induced chemical reactions and failure of materials from reactive FFs with fixed critical bond length or cut-offs can be problematic. In a future study, it would be interesting to see whether recently emerging neural network potentials can effectively handle this problem.

Supporting Information

The Supporting Information is available free of charge on the ACS Publications website.

Figures S1 – S11. Table S1 – S4. SMovies 1 – 12.

ORCID

Gang Seob Jung: 0000-0002-8047-6505

Stephan Irle: 0000-0003-4995-4991

Bobby G. Sumpter: 0000-0001-6341-0355

Notes

The authors declare that they have no competing financial interests. All data needed to evaluate the conclusions in the paper are present in the paper and/or the Supporting Information. Sample inputs and source codes to use DFTB+ with LAMMPS is shared in https://github.com/gsjung0419/DFTBP, which requires an updated API from the original DFTB+ package in https://github.com/gsjung0419/dftbplus). Additional data and example inputs related to this paper may be requested from the authors.

ACKNOWLEDGEMENTS

G.S.J. acknowledges support for developments by the Laboratory Directed Research and Development (LDRD) Program of Oak Ridge National Laboratory (Eugene P. Wigner Fellowship). This research used resources of the Compute and Data Environment for Science (CADES) at the Oak Ridge National Laboratory, which is supported by the Office of Science of the U.S. Department of Energy under Contract No. DE-AC05-00OR22725. G.S.J. and S.I. acknowledge support for parts of high temperature simulations and bond order analysis by Coal to Product (FWP No. FEAA155). BGS acknowledges work performed at Oak Ridge National Laboratory's Center for Nanophase Materials Sciences, a US Department of Energy Office of Science User Facilities.

TOC

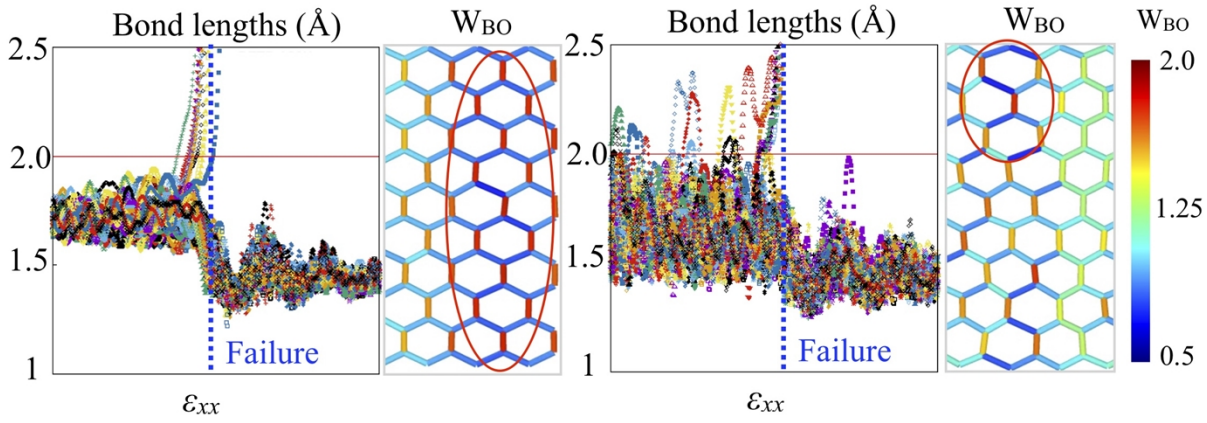

Low *T*=100K **High *T*=1000K**

REFERENCES

[1] M.J. Buehler, H. Gao, Dynamical fracture instabilities due to local hyperelasticity at crack tips, Nature 439(7074) (2006) 307-310.

[2] J.R. Kermode, T. Albaret, D. Sherman, N. Bernstein, P. Gumbsch, M.C. Payne et al., Low-speed fracture instabilities in a brittle crystal, Nature 455(7217) (2008) 1224-1227.

[3] A. Livne, E. Bouchbinder, I. Svetlizky, J. Fineberg, The Near-Tip Fields of Fast Cracks, Science 327(5971) (2010) 1359.

[4] A.A. Griffith, The phenomena of rupture and flow in solids, Phil, I Trans. R. Soc. Series A, 22L-I63-198 (1920-L92L) (1920).

[5] E. Bitzek, J.R. Kermode, P. Gumbsch, Atomistic aspects of fracture, International Journal of Fracture 191(1) (2015) 13-30.

[6] T. Zhang, X. Li, H. Gao, Fracture of graphene: a review, International Journal of Fracture 196(1) (2015) 1-31.

[7] H. Zhao, N.R. Aluru, Temperature and strain-rate dependent fracture strength of graphene, Journal of Applied Physics 108(6) (2010) 064321.

[8] M.A.N. Dewapriya, R.K.N.D. Rajapakse, A.S. Phani, Atomistic and continuum modelling of temperature-dependent fracture of graphene, International Journal of Fracture 187(2) (2014) 199-212.

[9] P. Liu, A.T. Liu, D. Kozawa, J. Dong, J.F. Yang, V.B. Koman et al., Autoperforation of 2D materials for generating two-terminal memristive Janus particles, Nature Materials 17(11) (2018) 1005-1012.

[10] G.H. Ryu, T. Zhu, J. Chen, S. Sinha, V. Shautsova, J.C. Grossman et al., Striated 2D Lattice with Sub-nm 1D Etch Channels by Controlled Thermally Induced Phase Transformations of PdSe2, Advanced Materials 31(46) (2019) 1904251.

[11] Y.-C. Lin, C. Liu, Y. Yu, E. Zarkadoula, M. Yoon, A.A. Puretzky et al., Low Energy Implantation into Transition-Metal Dichalcogenide Monolayers to Form Janus Structures, ACS Nano 14(4) (2020) 3896-3906.

[12] S. Wang, Z. Qin, G.S. Jung, F.J. Martin-Martinez, K. Zhang, M.J. Buehler et al., Atomically Sharp Crack Tips in Monolayer MoS2 and Their Enhanced Toughness by Vacancy Defects, ACS Nano 10(11) (2016) 9831-9839.

[13] G.S. Jung, S. Wang, Z. Qin, F.J. Martin-Martinez, J.H. Warner, M.J. Buehler, Interlocking Friction Governs the Mechanical Fracture of Bilayer MoS2, ACS Nano 12(4) (2018) 3600-3608.

[14] J. Chen, G.S. Jung, G.H. Ryu, R.-J. Chang, S. Zhou, Y. Wen et al., Atomically Sharp Dual Grain Boundaries in 2D WS2 Bilayers, Small 15(42) (2019) 1902590.

[15] G.S. Jung, S. Wang, Z. Qin, S. Zhou, M. Danaie, A.I. Kirkland et al., Anisotropic Fracture Dynamics Due to Local Lattice Distortions, ACS Nano 13(5) (2019) 5693-5702.

[16] Y. Han, M.-Y. Li, G.-S. Jung, M.A. Marsalis, Z. Qin, M.J. Buehler et al., Sub-nanometre channels embedded in two-dimensional materials, Nature Materials 17(2) (2018) 129-133.
[17] C. Daniels, A. Horning, A. Phillips, D.V.P. Massote, L. Liang, Z. Bullard et al., Elastic, plastic, and fracture mechanisms in graphene materials, Journal of Physics: Condensed Matter 27(37) (2015) 373002.
[18] M. Gaus, Q. Cui, M. Elstner, DFTB3: Extension of the Self-Consistent-Charge Density-Functional Tight-Binding Method (SCC-DFTB), Journal of Chemical Theory and Computation 7(4) (2011) 931-948.
[19] M. Tolladay, F. Scarpa, N.L. Allan, Interatomic forces breaking carbon-carbon bonds, Carbon 175 (2021) 420-428.
[20] S. Plimpton, Fast Parallel Algorithms for Short-Range Molecular Dynamics, Journal of Computational Physics 117(1) (1995) 1-19.
[21] B. Hourahine, B. Aradi, V. Blum, F. Bonafé, A. Buccheri, C. Camacho et al., DFTB+, a software package for efficient approximate density functional theory based atomistic simulations, The Journal of Chemical Physics 152(12) (2020) 124101.
[22] P. Giannozzi, S. Baroni, N. Bonini, M. Calandra, R. Car, C. Cavazzoni et al., QUANTUM ESPRESSO: a modular and open-source software project for quantum simulations of materials, Journal of Physics: Condensed Matter 21(39) (2009) 395502.
[23] P. Giannozzi, O. Andreussi, T. Brumme, O. Bunau, M. Buongiorno Nardelli, M. Calandra et al., Advanced capabilities for materials modelling with Quantum ESPRESSO, Journal of Physics: Condensed Matter 29(46) (2017) 465901.
[24] A. Dal Corso, Pseudopotentials periodic table: From H to Pu, Computational Materials Science 95 (2014) 337-350.
[25] P.E. Blöchl, Projector augmented-wave method, Physical Review B 50(24) (1994) 17953-17979.
[26] J.P. Perdew, K. Burke, M. Ernzerhof, Generalized Gradient Approximation Made Simple, Physical Review Letters 77(18) (1996) 3865-3868.
[27] Y. Baskin, L. Meyer, Lattice Constants of Graphite at Low Temperatures, Physical Review 100(2) (1955) 544-544.
[28] M. Elstner, D. Porezag, G. Jungnickel, J. Elsner, M. Haugk, T. Frauenheim et al., Self-consistent-charge density-functional tight-binding method for simulations of complex materials properties, Physical Review B 58(11) (1998) 7260-7268.
[29] M. Gaus, A. Goez, M. Elstner, Parametrization and Benchmark of DFTB3 for Organic Molecules, Journal of Chemical Theory and Computation 9(1) (2013) 338-354.
[30] V.Q. Vuong, Y. Nishimoto, D.G. Fedorov, B.G. Sumpter, T.A. Niehaus, S. Irle, The Fragment Molecular Orbital Method Based on Long-Range Corrected Density-Functional Tight-Binding, Journal of Chemical Theory and Computation 15(5) (2019) 3008-3020.

[31] I. Mayer, Bond order and valence indices: A personal account, Journal of Computational Chemistry 28(1) (2007) 204-221.
[32] S.G. Srinivasan, A.C.T. van Duin, P. Ganesh, Development of a ReaxFF Potential for Carbon Condensed Phases and Its Application to the Thermal Fragmentation of a Large Fullerene, The Journal of Physical Chemistry A 119(4) (2015) 571-580.
[33] B.D. Jensen, K.E. Wise, G.M. Odegard, Simulation of the Elastic and Ultimate Tensile Properties of Diamond, Graphene, Carbon Nanotubes, and Amorphous Carbon Using a Revised ReaxFF Parametrization, The Journal of Physical Chemistry A 119(37) (2015) 9710-9721.
[34] D.W. Brenner, O.A. Shenderova, J.A. Harrison, S.J. Stuart, B. Ni, S.B. Sinnott, A second-generation reactive empirical bond order (REBO) potential energy expression for hydrocarbons, Journal of Physics: Condensed Matter 14(4) (2002) 783-802.
[35] S.J. Stuart, A.B. Tutein, J.A. Harrison, A reactive potential for hydrocarbons with intermolecular interactions, The Journal of Chemical Physics 112(14) (2000) 6472-6486.
[36] J. Yeo, G.S. Jung, F.J. Martín-Martínez, J. Beem, Z. Qin, M.J. Buehler, Multiscale Design of Graphyne-Based Materials for High-Performance Separation Membranes, Advanced Materials 31(42) (2019) 1805665.
[37] Y. Chu, T. Ragab, P. Gautreau, C. Basaran, Mechanical Properties of Hydrogen Edge–Passivated Chiral Graphene Nanoribbons, Journal of Nanomechanics and Micromechanics 5(4) (2015) 04015001.
[38] J. Zhang, T. Ragab, C. Basaran, Comparison of fracture behavior of defective armchair and zigzag graphene nanoribbons, International Journal of Damage Mechanics 28(3) (2018) 325-345.
[39] G. Fiorin, M.L. Klein, J. Hénin, Using collective variables to drive molecular dynamics simulations, Molecular Physics 111(22-23) (2013) 3345-3362.
[40] I.V. Lebedeva, A.S. Minkin, A.M. Popov, A.A. Knizhnik, Elastic constants of graphene: Comparison of empirical potentials and DFT calculations, Physica E: Low-dimensional Systems and Nanostructures 108 (2019) 326-338.
[41] K.B. Wiberg, Application of the pople-santry-segal CNDO method to the cyclopropylcarbinyl and cyclobutyl cation and to bicyclobutane, Tetrahedron 24(3) (1968) 1083-1096.
[42] D. Moran, F. Stahl, H.F. Bettinger, H.F. Schaefer, P.v.R. Schleyer, Towards Graphite: Magnetic Properties of Large Polybenzenoid Hydrocarbons, Journal of the American Chemical Society 125(22) (2003) 6746-6752.
[43] P. Zhang, L. Ma, F. Fan, Z. Zeng, C. Peng, P.E. Loya et al., Fracture toughness of graphene, Nature Communications 5(1) (2014) 3782.
[44] G. Jung, Z. Qin, M.J. Buehler, Molecular mechanics of polycrystalline graphene with enhanced fracture toughness, Extreme Mechanics Letters 2 (2015) 52-59.

[45] S.L. Mayo, B.D. Olafson, W.A. Goddard, DREIDING: a generic force field for molecular simulations, The Journal of Physical Chemistry 94(26) (1990) 8897-8909.
[46] A.K. Rappe, W.A. Goddard, Charge equilibration for molecular dynamics simulations, The Journal of Physical Chemistry 95(8) (1991) 3358-3363.

Table 1. K-space grids and size for the inputs of the DFTB+ package for convergence tests under the static loading, which is prepared separately from the LAMMPS input file.

# Atoms	Size (Å)	K space	# OMP Threads
24	7.4 x 8.5	8x8x1/4x4x1/2x2x1/1x1x1	1
60	12.3 x 12.8	1x1x1/2x2x1	1
112	17.2 x 17.0	1x1x1/2x2x1	2
160	19.7 x 21.3	1x1x1	4
240	24.6 x 25.6	1x1x1	8

Table 2. Elastic constants obtained from DFTB and molecular mechanics simulations.

	E (GPa)	$(C_{11}-C_{12})/2$ (GPa)	ν
DFT[40]	1010		0.203
DFTB (3OB)	1108.2	451.9	0.226
AIREBO	828.8	304.1	0.362
ReaxFF	787.2	256.2	0.536

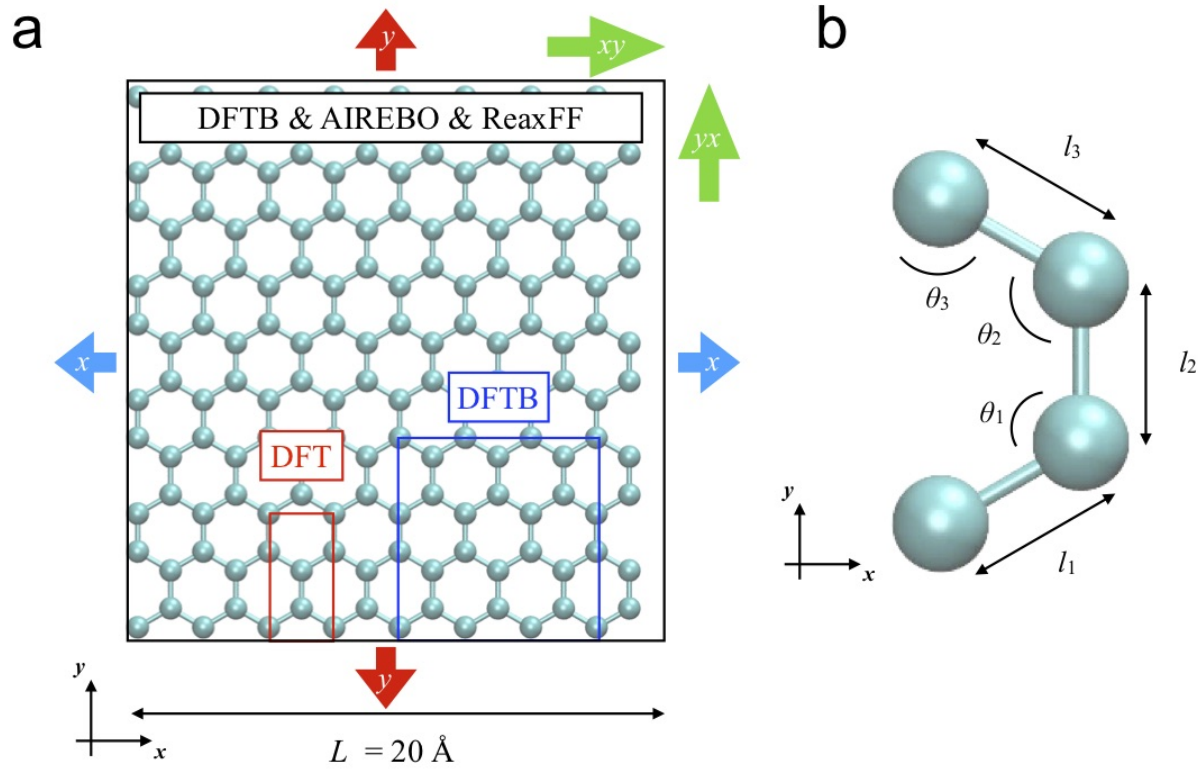

Figure 1 (**a**) The graphene sizes of tested systems with different DFT, DFTB, and reactive FFs methods under various loading conditions (*x*, *y*, *xy*, and *yx*). Only four atoms are included in DFT (red) calculations, and 24 atoms are included in DFTB (blue) for different parameters. To directly compare the mechanical behaviors of FFs and DFTB, we use 160 atoms in the system after checking the size effects in DFTB. (**b**) The definition of three different bond lengths and angles to compare the deformation obtained from DFT, DFTB, and FFs.

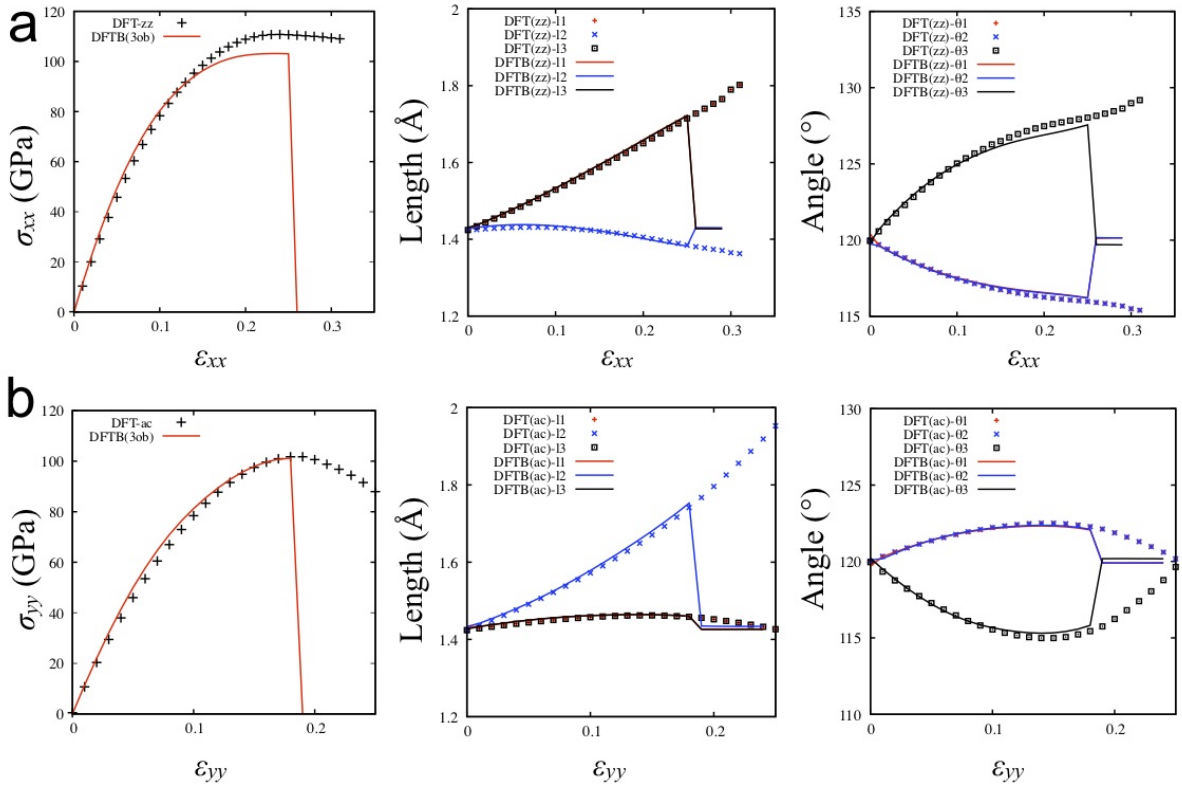

Figure 2 Stress-strain curves and deformation under tensile loadings along the *x* (zz: zigzag) and *y* (ac: armchair) directions; three different bonds and angles of graphene from the DFTB and DFT calculations. The DFT data are calculated from the static loading, and the DFTB data are obtained from the quasi-static loading to capture the failure points. The systematic comparisons for the different loading conditions described in Methods. See Movies 1 and 2 for the charge density change during the tensile loading.

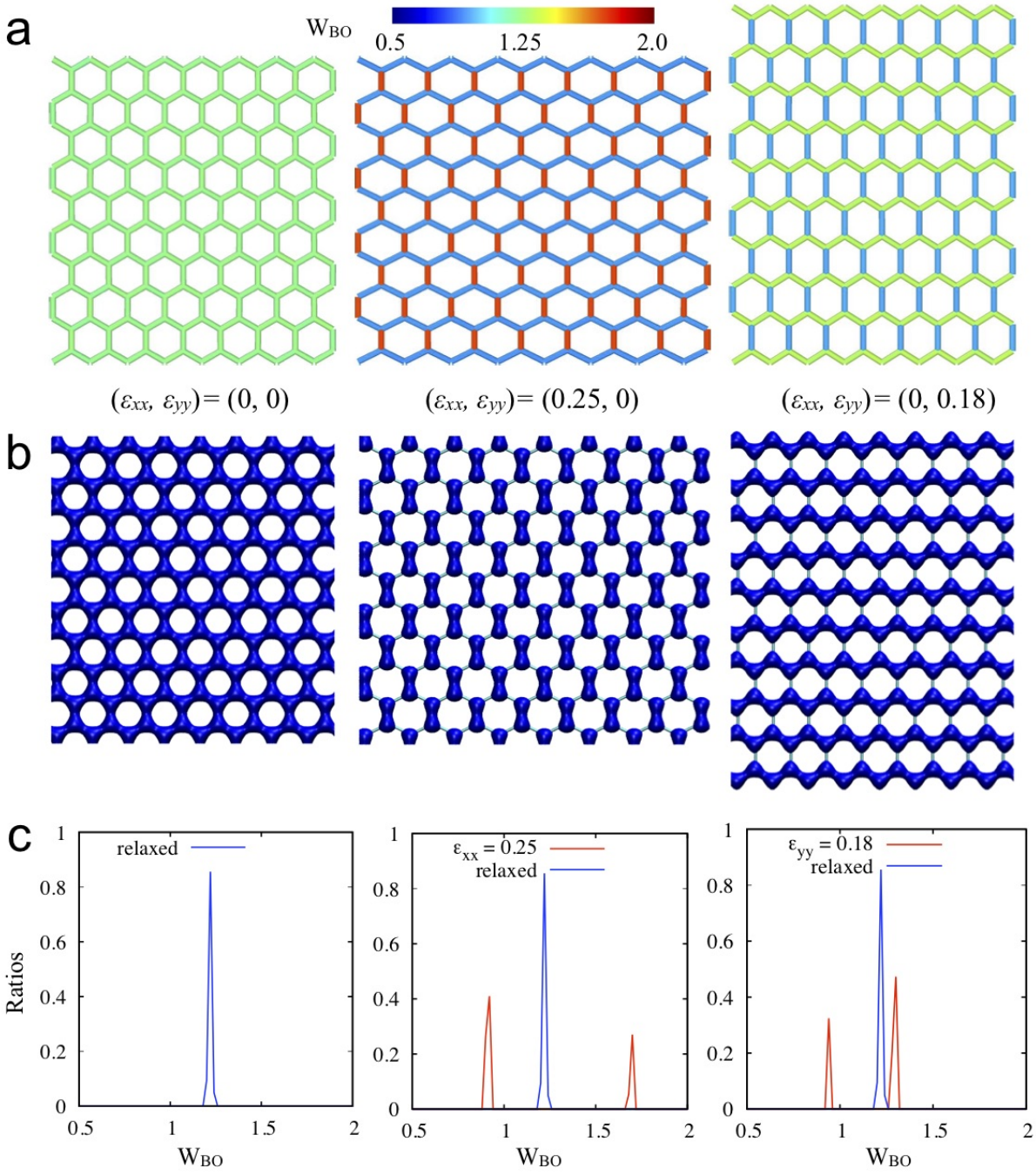

Figure 3 Distribution of Wiberg bond order (**a**) and charge density (**b**) under maximum tensile strain during the quasi-static loading along the *x* (zz: zigzag) and *y* (ac: armchair) directions compared to the relaxed system. (**c**) Ratios of bonds with the different values of bond orders. It clearly shows that there is a transition from sp^2 hybridization to single bond where the bond breaking initiates (See SMovies 1-4).

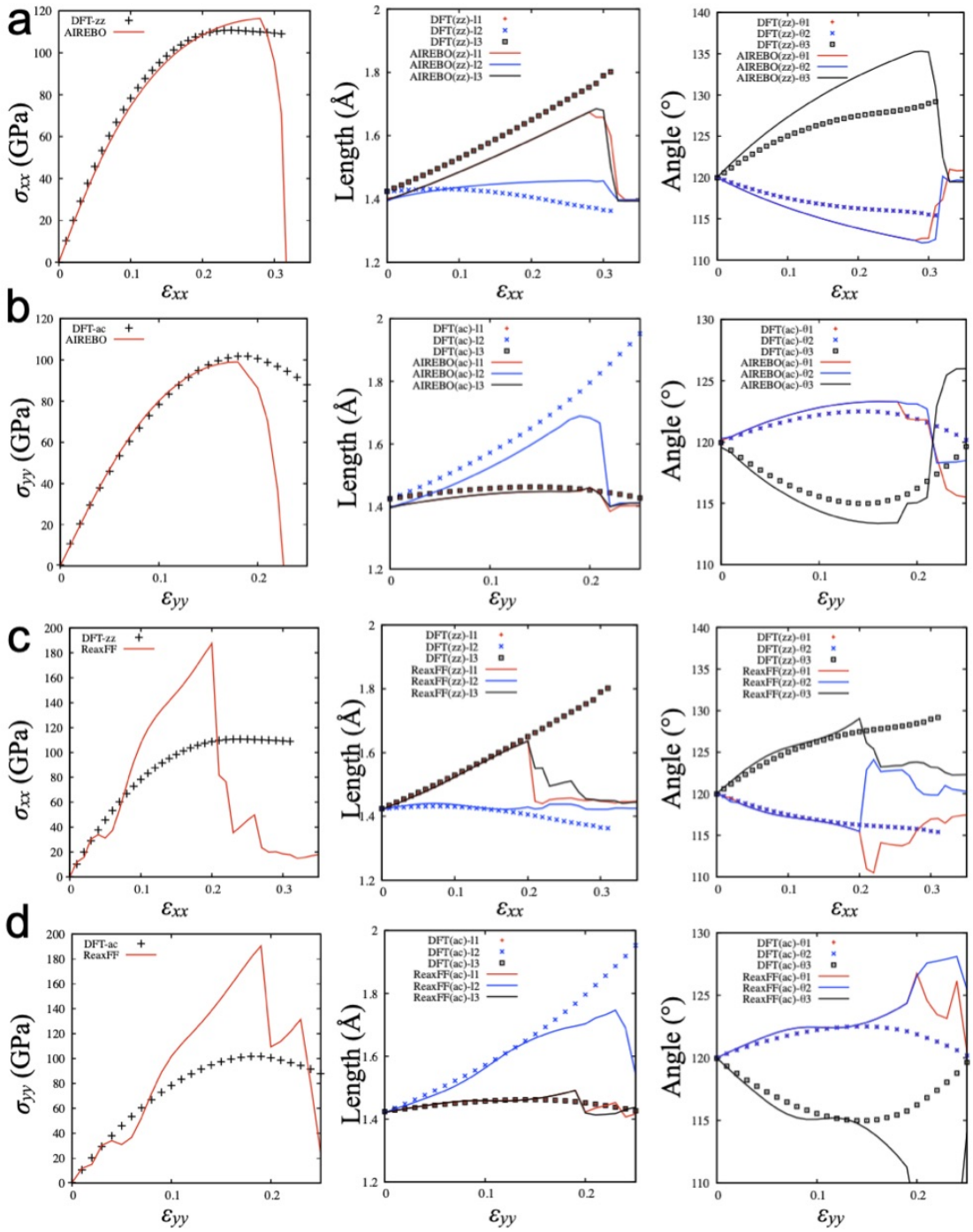

Figure 4 Stress-strain curves and deformation under tensile loadings along the *x* (zz: zigzag) and *y* (ac: armchair) directions; three different bonds and angles of graphene from AIREBO (**a**, **b**), ReaxFF-C_{2013} (**c**, **d**) and DFT calculations. The DFT data are obtained from the static loading, and AIREBO and ReaxFF data are derived from the quasi-static loading to capture the failure points.

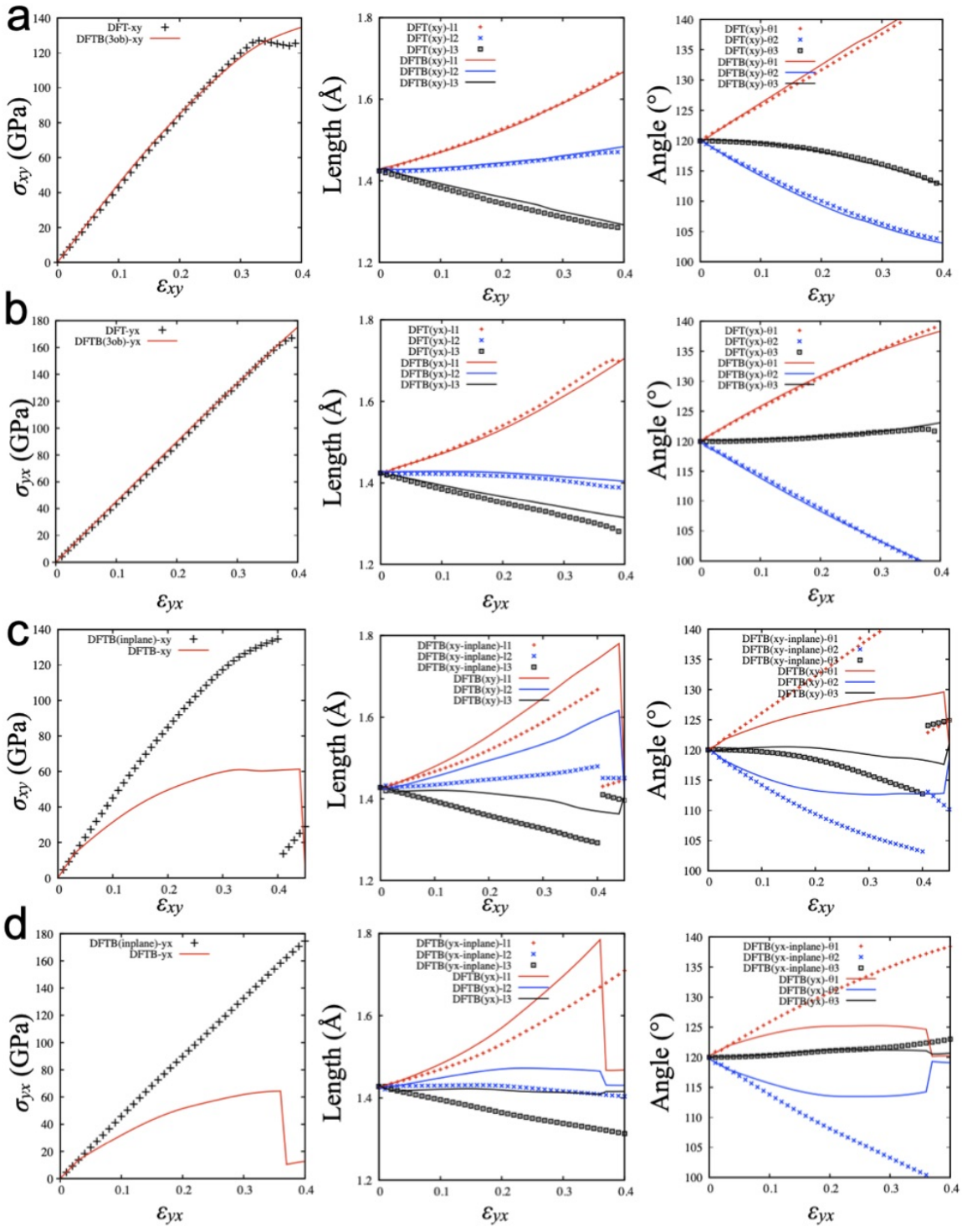

Figure 5 Stress-strain curves and deformation under shear loadings along the *xy* and *yx* directions; Three different bonds and angles of graphene from DFTB and DFT calculations. To correctly compare the behaviors with DFT calculations, the out-of-plane deformation is restricted in the *xy* plane (**a**, **b**) while the others are calculated without the restrictions (**c**, **d**).

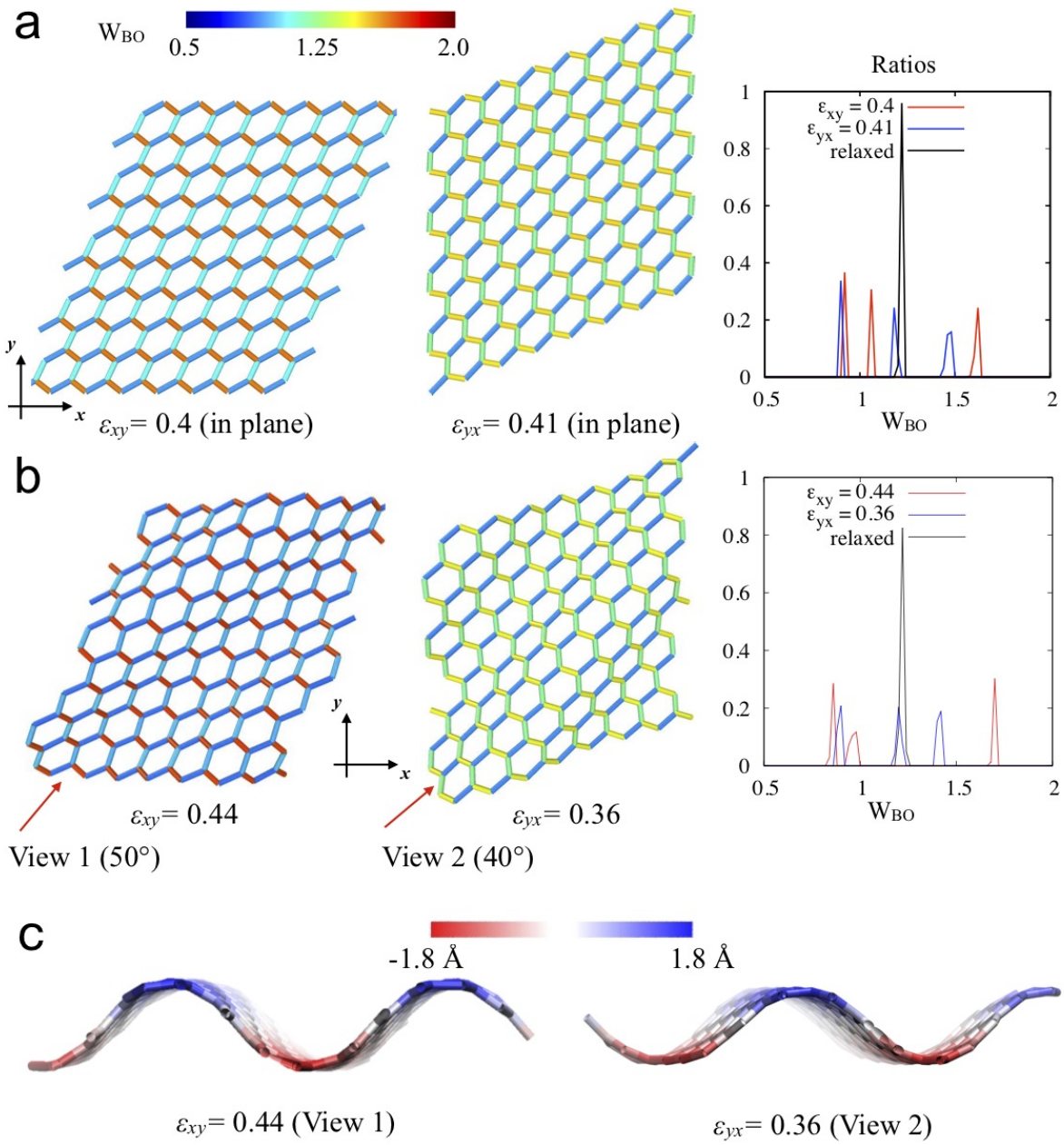

Figure 6 Distribution of Wiberg's bond order under shear loadings along the *xy* and *yx* directions from quasit-static loading with DFTB. (**a**) The out-of-plane deformation is not allowed while wrinkling is allowed in **b**. (**c**) The sides views of rippled graphene due to the shear loading as indicated in panel **b**.

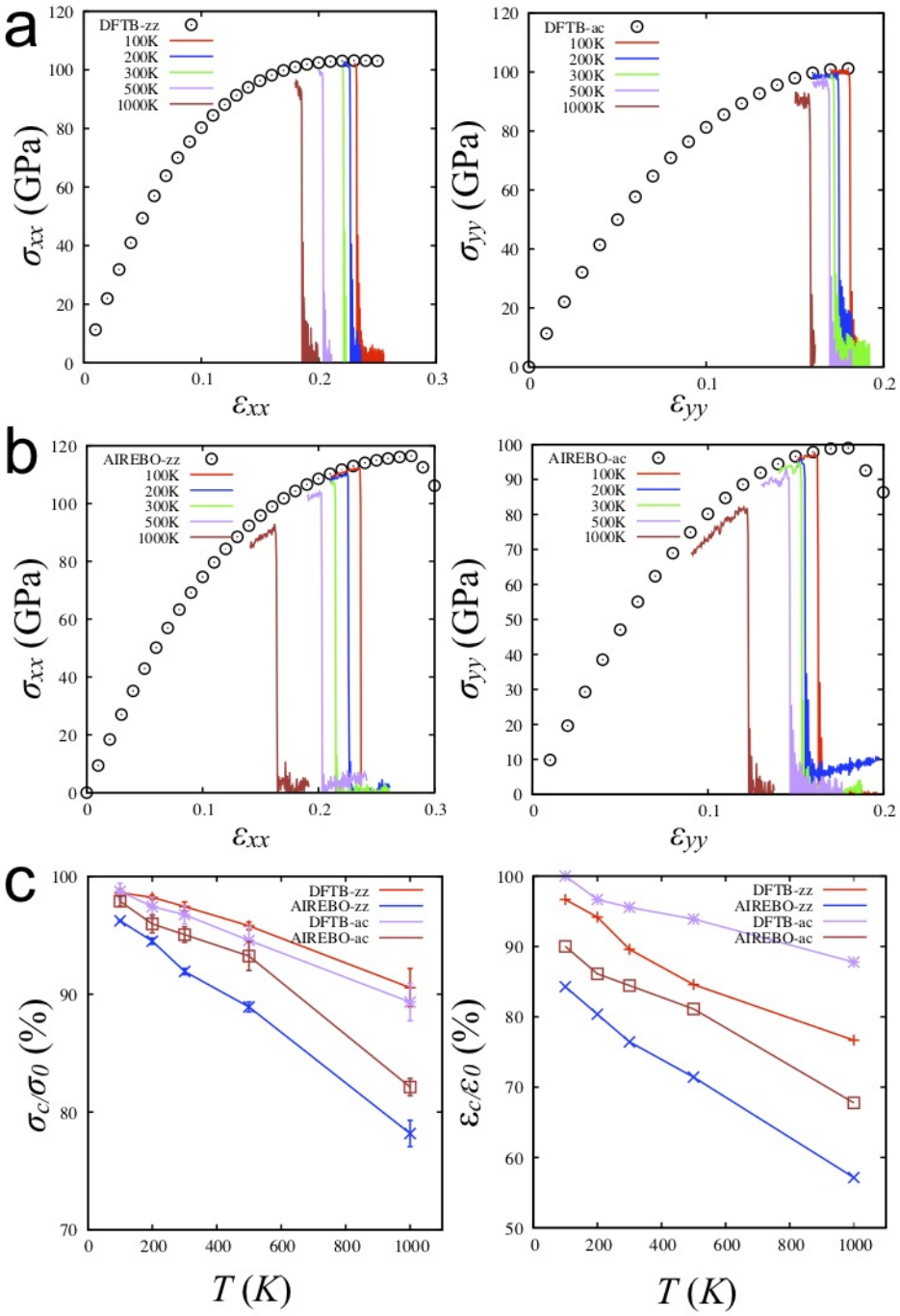

Figure 7 Stress-strain curves from DFTB (**a**) and AIREBO (**b**) with different temperature under quasi-dynamic loading along with the *zz* and *ac* directions. (**c**) Summary of critical strength and strains compared to the values under the quasi-static loading.